Advanced Powder Materials 3 (2024) 100242

Contents lists available at ScienceDirect

Advanced Powder Materials

journal homepage: www.keaipublishing.com/en/journals/advanced-powder-materials

Green and regulable synthesis of CdNCN on CdS semiconductor: Atomic-level heterostructures for enhanced photocatalytic hydrogen evolution

Taiyu Huang [a,1], Zimo Huang [b,1], Xixian Yang [a,**], Siyuan Yang [a], Qiongzhi Gao [a], Xin Cai [a], Yingju Liu [a], Yueping Fang [a], Shanqing Zhang [b,c,***], Shengsen Zhang [a,*]

[a] College of Materials and Energy, South China Agricultural University, Guangzhou 510643, China
[b] Institute for Sustainable Transformation, School of Chemical Engineering and Light Industry, Guangdong University of Technology, Guangzhou 510006, China
[c] Centre for Clean Environment and Energy, and School of Environment and Science, Gold Coast Campus, Griffith University, Queensland 4222, Australia

ARTICLE INFO

Keywords:
CdNCN semiconductor
CdS
Photocatalytic hydrogen production
Atomic-level interface engineering
Electron transfer pathway

ABSTRACT

In the realm of photoenergy conversion, the scarcity of efficient light-driven semiconductors poses a significant obstacle to the advancement of photocatalysis, highlighting the critical need for researchers to explore novel semiconductor materials. Herein, we present the inaugural synthesis of a novel semiconductor, CdNCN, under mild conditions, while shedding light on its formation mechanism. By effectively harnessing the $[NCN]^{2-}$ moiety in the thiourea process, we successfully achieve the one-pot synthesis of CdNCN-CdS heterostructure photocatalysts. Notably, the optimal CdNCN-CdS sample demonstrates a hydrogen evolution rate of 14.7 mmol g^{-1} h^{-1} under visible light irradiation, establishing itself as the most efficient catalyst among all reported CdS-based composites without any cocatalysts. This outstanding hydrogen evolution performance of CdNCN-CdS primarily arises from two key factors: i) the establishment of an atomic-level N-Cd-S heterostructure at the interface between CdNCN and CdS, which facilitating highly efficient electron transfer; ii) the directed transfer of electrons to the (110) crystal plane of CdNCN, promoting optimal hydrogen adsorption and active participation in the hydrogen evolution reaction. This study provides a new method for synthesizing CdNCN materials and offers insights into the design and preparation of innovative atomic-level composite semiconductor photocatalysts.

1. Introduction

Solar-driven photocatalytic water splitting processes, being a focal area of research in addressing energy challenges, are considered a promising avenue for renewable energy production owing to their sustained energy supply and environmentally friendly production methods [1]. Over the past five decades, researchers have endeavored to explore numerous semiconductor materials (including metal oxides, metal sulfides, organic semiconductors, etc.) for photocatalytic hydrogen production [2–4]. However, the current photocatalysts have not yet achieved the required efficiency for practical applications due to factors such as bandgap width, chemical stability, and rapid carrier recombination. Therefore, the exploration of novel semiconductors that align with the core principles of photocatalysis is paramount in the development process of photocatalysis [5–7]. CdNCN, a novel transition metal carbodiimide compound, has attracted significant attention due to its favorable band gap and excellent photoelectric response [8]. This compound predominantly coordinates with Cd^{2+} ions through the nitrogen atom of the carbodiimide group $[N{=}C{=}N]^{2-}$ (denoted as $[NCN]^{2-}$), forming an organic-inorganic hybrid structure [9,10]. The two relatively electronegative nitrogen atoms and the electrophilic carbon center constitute the chemically soft carbodiimide group. This results in a shift in electron cloud density during coordination, leading to an overall stronger covalent state in CdNCN [11].

* Corresponding author.
** Corresponding author.
*** Corresponding author. Institute for Sustainable Transformation, School of Chemical Engineering and Light Industry, Guangdong University of Technology, Guangzhou 510006, China.
E-mail addresses: yangxixian@yeah.net (X. Yang), s.zhang@griffith.edu.au, s.zhang@gdut.edu.cn (S. Zhang), zhangss@scau.edu.cn (S. Zhang).
[1] These authors contributed equally to this work.

https://doi.org/10.1016/j.apmate.2024.100242
Received 7 August 2024; Received in revised form 7 September 2024; Accepted 14 September 2024
Available online 26 September 2024

Due to the strong recombination of electron-hole pairs within semiconductors, the photocatalytic efficiency of a single semiconductor is relatively low. Therefore, constructing heterojunction structures to accelerate the separation of electron-hole pairs can enhance the overall photocatalytic efficiency [12–14]. Currently, significant efforts have been devoted to constructing heterojunction structures capable of suppressing charge carrier recombination. For example, Huang et al. achieved enhanced carrier separation within the semiconductor by in-situ growth of CdS on MXene [15]. Additionally, Kawi et al. By designing a Cd atomic layer between CdS and Co_9S_8, the transfer of electrons from CdS/Co_9S_8 to Cd atoms can be accelerated [16]. However, constrained by the different atomic affinities at the heterojunction interface, transition structures still suffer from loose binding, resulting in hindered carrier transport at the heterojunction interface. Therefore, assembling different crystals constructed from the same element to form heterostructures (such as CdNCN-CdS: NCN-Cd-S-Cd) and utilizing the excellent atomic affinity to construct "quasi-crystalline" transition sites to accelerate carrier transport is feasible approach. In heterojunction system, by utilizing the electron attraction characteristics of the $[NCN]^{2-}$ group in CdNCN, it is possible to facilitate directed migration of photoexcited carriers within the heterostructures, establishing an effective electron transfer pathway and thus improving the separation efficiency of photogenerated carriers. Therefore, the development of composite heterostructure photocatalysts based on CdNCN holds significant potential. Currently, the synthesis methods for CdNCN primarily involve solid-state decomposition or liquid-phase injection techniques, which necessitate stringent conditions such as oxygen isolation in a glove box or the use of highly toxic substances like cyanamide [10]. Addressing the challenge of developing a controlled synthesis method for CdNCN and its heterostructures under milder conditions remains crucial.

As a sulfur-containing compound, thiourea, benefiting from its rapid desulfurization kinetics and simple molecular formula, is commonly used as a key precursor for synthesizing CdS [17,18]. However, in current research on CdS synthesis, the focus primarily lies on utilizing high-temperature and high-pressure solvothermal methods to induce the decomposition of thiourea, ultimately obtaining CdS crystals. While this process accelerates the decomposition of thiourea to yield pure CdS nanomaterials, it overlooks the bonding of other by-products formed during the thiourea decomposition process with Cd^{2+} ions. Based on Valenzuela's speculation, it is inferred that different directional decomposition products will be generated during the thiourea decomposition process [19]. However, there is currently no research confirming the mechanism of thiourea's final products utilization. These uncertainties obscure the thiourea decomposition process and its products, and the production of CdNCN has been long overlooked. Therefore, it is crucial to monitor and determine the mechanism of thiourea decomposition and obtain CdNCN materials to gain a deeper understanding of the utilization mechanism of thiourea.

Herein, we present a novel mechanism for utilizing thiourea, enabling the one-pot synthesis of efficient CdNCN-CdS integrated photocatalysts under mild conditions. By precisely adjusting the ratio of the Cd source and thiourea during synthesis, we control the composition and microstructure of the composite catalyst. The formation mechanism of CdNCN is elucidated using in-situ Fourier transform infrared spectroscopy (FT-IR) analysis. Further insights are gained through in situ and ex situ X-ray photoelectron spectroscopy (XPS) tests and electron localization function (ELF) calculations, which reveal that the $[NCN]^{2-}$ moiety in the heterostructure forms a rapid electron transfer pathway among N-Cd-S, tightly binding with the Cd atoms in CdS. In-situ atomic force microscopy-Kelvin probe force microscopy (AFM-KPFM) testing under light illumination confirmed the direction of electron transport in the heterogeneous photocatalyst. Steady-state fluorescence testing and femtosecond transient absorption spectroscopy (fs-TAS) determined that the binding of CdNCN-CdS suppressed the fluorescence emission of CdNCN, thereby accelerating carrier separation and ultimately determining the direction of carrier migration in the sample. Moreover, through hydrogen adsorption energy calculations, we identified optimal hydrogen desorption sites on different crystal planes of CdNCN, elucidating charge transfer and hydrogen evolution pathways. This study validates that the CdNCN-CdS composite sample adeptly constructs atomic-level heterostructure interfaces at the interface, consequently markedly enhancing the overall efficiency of hydrogen production.

2. Results and discussion

Recent literature reports on the synthesis of CdNCN are limited, with only Dronskowski and Huang et al. noted for their contributions [8,10]. However, their methods, which involve solid-state metathesis reactions and liquid-phase injection, necessitate stringent conditions and the use of highly toxic substances. In contrast, our research presents a novel approach utilizing the thiourea moiety for a one-step synthesis of CdNCN-CdS structures by elucidating the generation of $[NCN]^{2-}$ moieties during thiourea decomposition and employing a gradient concentration method to judiciously utilize $[NCN]^{2-}$ moieties, we achieved the controllable one-step synthesis of CdNCN-CdS structures. Prevailing research indicates that heating thiourea in an alkaline environment intensifies the stretching vibrations of the C=S chemical bond, leading to its decomposition and subsequent release of S^{2-} which then react with Cd^{2+} to form CdS [20,21]. However, there are discrepancies in reports about subsequent reaction processes and products [22]. Here, as depicted in Fig. 1a–i and Fig. S1, our study employs in-situ FT-IR to monitor real-time thiourea decomposition in water (Light yellow indicates weak or near-zero intensity vibrations, while deep purple represents strong vibrations). As the temperature increases from 298 K to 333 K, the intensity of the –OH (H_2O) stretching band at 3200 cm^{-1} decreases, and its frequency shifts towards higher values, which is consistent with previous work [23]. The vibrational intensity of the C=S bond at 1190 cm^{-1} rapidly diminishes within a frame of 20 min upon reaching a temperature of 333 K, as shown in Fig. 1a–ii. Subsequently, after maintaining this temperature for an additional duration of 20 min, the characteristic peak associated with the C=S bond nearly disappears, indicating cleavage of the C=S bond in thiourea in the heated aqueous environment (Equation (1)) [24]. Meanwhile, the vibrational peak corresponding to the C-N bond at 1230 cm^{-1} gradually emerges and continues to intensify until it reaches its maximum intensity towards the end of a period lasting approximately 50 min (Fig. 1a–iii) [25]. The infrared feature peak of the C–N bond decreases rapidly after 50 min and nearly vanishes around 80 min, suggesting that all thiourea has progressed to the second stage of the reaction, resulting in the formation of $\cdot[CN_2H_2]$ and ultimately $[NCN]^{2-}$ as described by Equations (2) and (3). The asymmetric stretching vibration peak at 2278 cm^{-1} signals the presence of N–C≡N, indicative of the intermediate $\cdot[CN_2H_2]$ formation [22,26]. As time progresses, the intensity of this N–C≡N stretching vibration peak increases, signaling a higher concentration of intermediate products and facilitating the formation of $[NCN]^{2-}$ (Fig. 1a–vi). Moreover, the symmetric stretching vibration peak attributed to N=C=N around 2130 cm^{-1} is shielded due to the influence of water's associational bands.

$$(NH_2)_2CS \leftrightarrow H_2S + \cdot[CN_2H_2] \quad (1)$$

$$[CN_2H_2] \leftrightarrow [NCN]^{2-} + 2H^+ \quad (2)$$

$$2Cd^{2+} + (NH_2)_2CS + 4OH^- \xrightarrow{\Delta} CdS + CdNCN + 4H_2O \quad (3)$$

In this study, we employed a combination of experimental product characterization and theoretical calculations to collectively validate the presence of the N=C=N group [27]. Bond dissociation energy (BDE) calculations were utilized to evaluate the energy required for chemical bond cleavage during thiourea decomposition, revealing a detailed mechanism through optimized simulation processes [28]. The initial step of thiourea decomposition, as illustrated in Fig. 1b, primarily involves

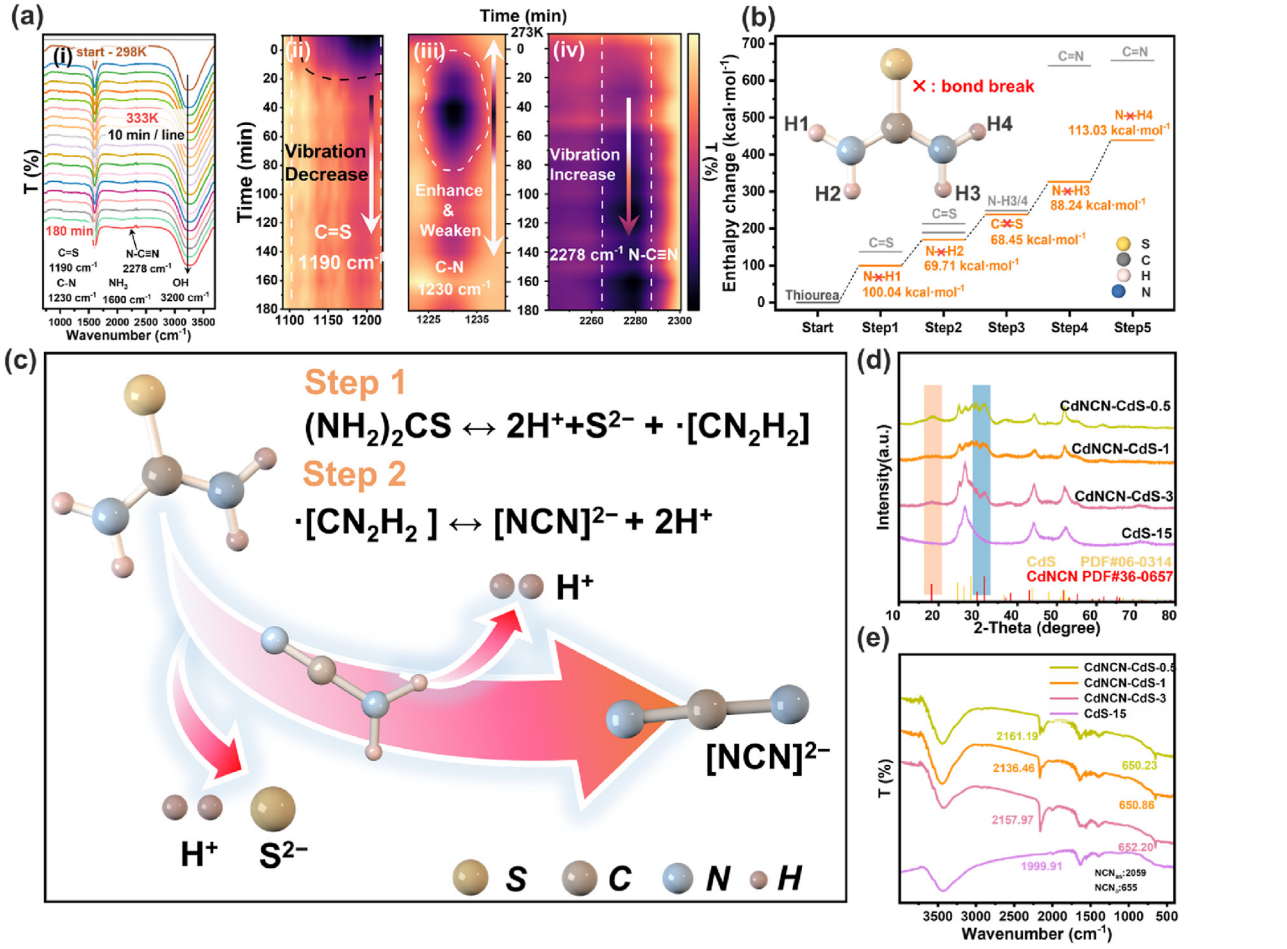

Fig. 1. (a) In-situ FT-IR of thiourea heated in aqueous solution: (i) survey spectrum, (ii) variation of C=S bond intensity at 1190 cm^{-1} with time, (iii) variation of C–N bond intensity at 1230 cm^{-1} with time, (iv) variation of N–C≡N bond intensity at 2278 cm^{-1} with time (heating conditions: 298 K–333 K, duration at 333 K: 180 min); (b) Calculation of thiourea bond dissociation energy; (c) Mechanism diagram of the decomposition of thiourea to produce CdNCN and CdS; (d,e) XRD spectra (d) and FT-IR spectra (e) of CdNCN-CdS and pure CdS samples.

cleavage of the side-chain N-H bond, which necessitates lower energy compared to breaking the C=S bond. This initial cleavage induces an internal charge imbalance that facilitates subsequent rupture of the C=S bond and lead to the formation processes outlined in Equation (1). Further decomposition of ·[CN_2H_2] reveals that cleaving N-H bonds requires less energy than breaking C=N bonds, resulting in the formation of the final $[NCN]^{2-}$ moiety (Equation (2)). Single-point energy and VSAP calculations for structural energy changes corroborate these findings (Figs. S2–S3). These calculations indicate that the C=S bond is more susceptible to cleavage, releasing S^{2-}, while decomposition of the [(NH_2)CN] group occurs at a slower rate. This difference significantly influences the sequential formation of CdS and CdNCN during the synthesis. Contrary to previous reports, our study finds that ·[CN_2H_2] does not merely lose an H^+ ion to form an N-C≡N structure [29]. Due to the moderate Pearson hardness of Cd^{2+}, the ·[CN_2H_2] formed after dehydrogenation binds to Cd^{2+} in a spatially symmetrical double bond structure, forming an organometallic ligand for the transition metal [10,30]. Meanwhile, in the presence of excess metal ions in the solution, S^{2-} initially dissociates on a temporal scale, interacting with Cd^{2+} to form CdS. Subsequently, the further dissociation of $[NCN]^{2-}$ moieties binds with the remaining Cd^{2+}, ultimately leading to the production of CdNCN. Thus, under specific heating conditions, the reaction between Cd^{2+}, thiourea, and OH^- can simultaneously produce CdNCN and CdS (Equation (3)). The proportions of these products can be controlled by adjusting the reaction conditions and the ratio of Cd^{2+} to thiourea. The dissociation process is schematically illustrated in Fig. 1c and Fig. S4.

By adjusting the $CdCl_2$ to thiourea ratio to 1:0.5, 1:1, 1:3, and 1:15, we synthesized four samples including three types of CdNCN-CdS and a pure CdS. These samples are denoted as CdNCN-CdS-0.5, CdNCN-CdS-1, CdNCN-CdS-3 and CdS-15 respectively. As depicted in Fig. 1d, the X-ray powder diffraction (XRD) characteristic peaks of CdS were clearly observed at 24.8°, 26.5°, and 28.2° for all samples (PDF#06–0314). Notably, the intensities of the crystalline diffraction peaks at 18.2° and 31.6°, corresponding to the (100) and (110) crystal planes of CdNCN (PDF#36–0657), exhibited enhancement with decreasing thiourea ratio. Fourier-transform infrared spectroscopy (FT-IR) was performed to identify. the types of organic ligands in CdNCN. In Fig. 1e, the σ deformation vibration of the N=C=N group at 650 cm^{-1} was clearly observable in all CdNCN-CdS samples. A strong asymmetric vibration at 2100 cm^{-1}, which is characteristic of carbodiimide groups in infrared spectra, was also evident. Interestingly, the absence of the symmetric stretching vibration typically associated with the $[N{\equiv}C{-}N]^{2-}$ moiety at 1230 cm^{-1} in the CdNCN-CdS samples suggests that the CdNCN is composed of $[N{=}C{=}N]^{2-}$ organic ligands rather than $[N \equiv C\text{-}N]^{2-}$ [10].These characterization results from XRD and FT-IR confirm that a novel CdNCN-CdS composite material with tunable proportions can be successfully synthesized in a one-step process by adjusting the ratio of thiourea to Cd source material. Concomitantly, ammonia molecules within the reaction milieu can coordinate with Cd^{2+} ions, thereby generating ammonia-metal complexes. This complexation process retards the precipitation of metal ions, facilitating the comprehensive reaction between the $[NCN]^{2-}$ moieties, which possess comparatively sluggish dissociation

rates, and Cd^{2+} ions from the solution on the CdS crystal nuclei, ultimately resulting in the formation CdNCN nanosheets. To further investigate this phenomenon, we utilized NaOH as a substitute for ammonia solution to modulate the pH of the reaction system. XRD results indicate that at pH = 11, neither ammonia nor sodium hydroxide has an effect on the generation of the final product $[NCN]^{2-}$ (Fig. S5). However, the faster release of metal ions in NaOH solution accelerates the overall reaction rate, leading to a more compacted structure in the final sample rather than nanosheet morphology (Fig. S6). Furthermore, considering the environmental impact of Cd^{2+}, the actual yield of the catalyst was evaluated. As shown in Tables S1–2 and Fig. S7, the catalyst yield in this experiment was approximately 86.3 %. Additionally, attempts were made to reuse the residual reaction solution. As depicted in Fig. S8, the secondary solution had minimal impact on the generation of the CdNCN-CdS catalyst, demonstrating the reusability of the solution post-reaction.

The microstructure of CdNCN-CdS and pure CdS samples was examined using scanning electron microscopy (SEM). As shown in Fig. 2a, the CdNCN-CdS-0.5 exhibited nanosheets with a stacked morphology consisting of multiple layers. This can be attributed to an insufficient amount of thiourea, where the dissociation rates of S^2 and $[NCN]^{2-}$ during the reaction process do not exhibit a significant temporal gradient concentration difference. The synchronous generation of CdS and CdNCN impedes CdS from serving as the growth nucleus for CdNCN, resulting in a less compact binding between the generated CdNCN and CdS. As the molar ratio of thiourea increases, the.

CdNCN nanosheets gradually thin out in the CdNCN-CdS-1 sample. In this configuration, CdS nanoparticles serve as crystal nuclei and structural supports between CdNCN layers, effectively inhibiting the aggregation of CdNCN nanosheets. In the CdNCN-CdS-3 sample, more Cd^{2+} react with S^{2-} to form CdS, leading to a reduction in the size of CdNCN nanosheets. To further validate the differences in microstructures, we conducted BET analysis to measure the specific surface area of the CdNCN-CdS-0.5, CdNCN-CdS-1, and CdNCN-CdS-3 samples. As shown in Fig. S9, among the three samples, CdNCN-CdS-1 exhibited the largest specific surface area. This is because the optimal Cd:thiourea ratio in CdNCN-CdS-1 prevents excessive stacking or breakage of the nanosheets, resulting in a more favorable microstructure. With further increases in the thiourea molar ratio (1:6, 1:8, and 1:10), the yield of CdNCN continues to decrease until eventually leading to complete disappearance of the nanosheet structure observed in SEM images (see Fig. S10). Thus, by controlling the molar ratio of Cd^{2+} to thiourea, precise manipulation of the composite catalyst components can be achieved, thereby effectively influencing the ratio and morphology of CdNCN and CdS within the CdNCN-CdS photocatalyst. Fig. 2b provides a more explicit illustration of the significant differences in composition and microstructure of the products obtained at varying ratios of $CdCl_2$ to thiourea.

High-resolution transmission electron microscopy (HRTEM) images

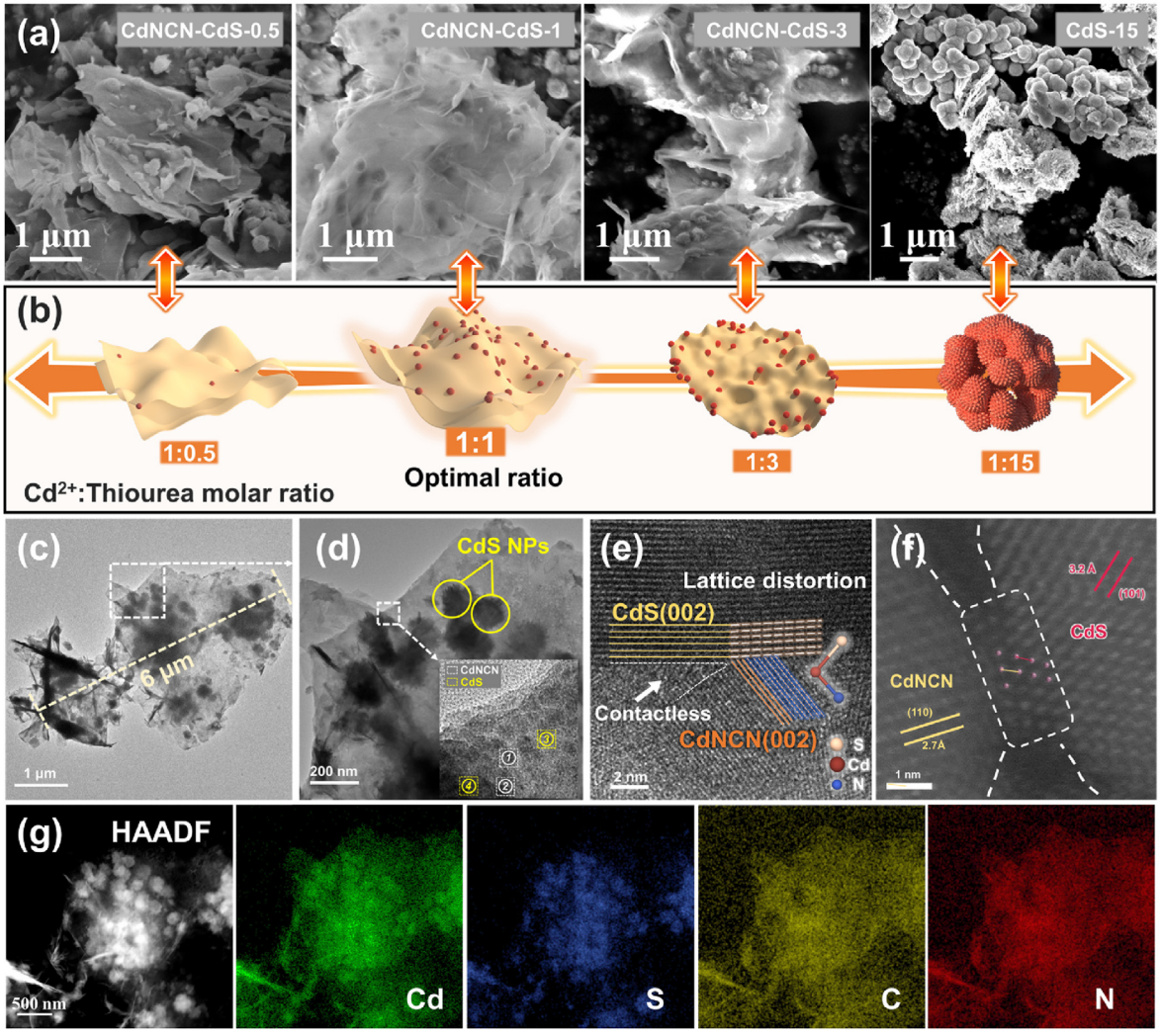

Fig. 2. (a) SEM images of CdNCN-CdS and pure CdS samples; (b) Schematic illustration of the microstructural changes induced by different $CdCl_2$ and thiourea molar ratios; (c–e) HRTEM images; (f) AC-STEM image; (g) HAADF image and TEM-EDS mapping of CdNCN-CdS-1 heterostructures photocatalyst.

of the CdNCN-CdS-1 sample, depicted in Fig. 2c and d, confirm its unique sheet-ball composite structure morphology. The nanosheets are approximately 6 μm in size, while the nanoparticles have a diameter ranging from 100 to 200 nm. Detailed HRTEM analysis at the interface between the nanoparticles and nanosheets, including their magnified views (Fig. S11), clearly reveals the distinct lattice spacings. Notably, Fig. 2e and Fig. S12 illustrates significant lattice distortion at the interface between CdNCN and CdS, indicating the presence of transition sites with N-Cd-S, which is further confirmed through subsequent XPS characterization. To verify the existence of an atomic-level heterojunction, AC-STEM was used to observe the CdNCN-CdS composite heterostructure interface (Fig. 2f). The measured lattice spacings on either side of the transition structure were 2.7 Å and 3.2 Å, corresponding to the (110) crystal plane of CdNCN and the (101) crystal plane of CdS, respectively. Notably, the spatial distance between Cd atoms at the heterojunction was elongated due to the larger spatial size of the $[NCN]^{2-}$ group compared to S^{2-} (Fig. S13). TEM/energy-dispersive spectroscopy (TEM–EDS) mapping on the CdNCN-CdS-1 sample reveals a distribution mapping of elements, as shown in Fig. 2g, demonstrating a widespread distribution of the Cd element throughout the structure with a primary concentration of the S element within observed nanoparticle regions in HAADF images. The uniform distribution of C and N elements enhances the distinctive characteristics of the CdNCN nanosheets. Further detailed elemental ratio analyses are available in the TEM-EDS data (Fig. S14). In contrast,

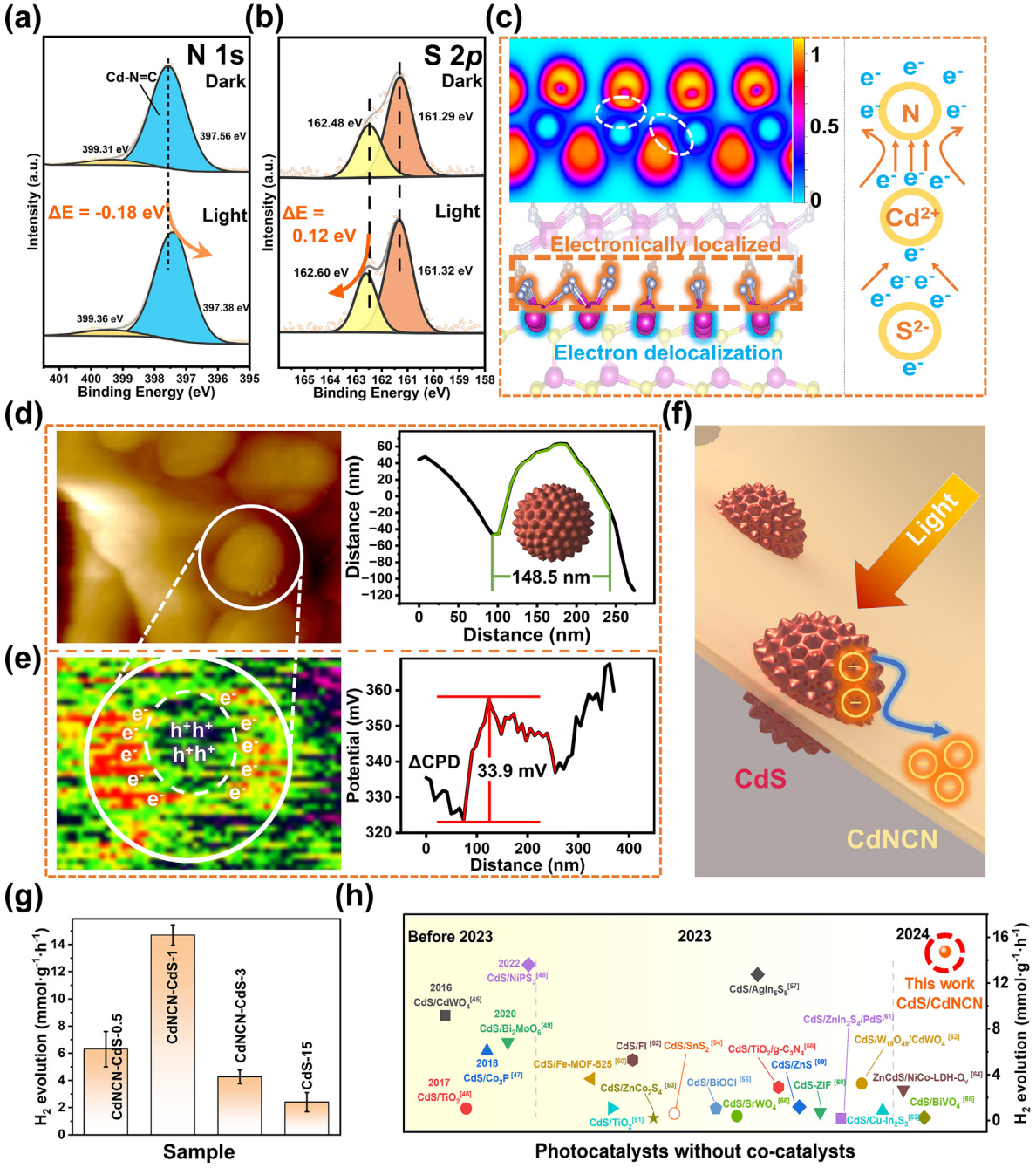

Fig. 3. In-situ XPS of the CdNCN-CdS-1sample under light and dark conditions: (a) N 1s; (b) S 2p; (c) Electron localization function calculation graph and schematic, where blue represents electron delocalization and yellow represents electron localization; (d) AFM test image of the CdNCN-CdS-1 sample; (e) KPFM contact potential difference test under irradiation; (f) Schematic illustration of electron transfer in CdNCN-CdS; (g) Comparative hydrogen production efficiency of different samples ($\lambda > 420$ nm); (h) Comparative hydrogen evolution efficiency of different CdS-based heterojunction systems.

HRTEM analysis of the CdS-15 sample confirms the predominant presence of pure CdS nanoparticles (Fig. S15). The catalyst and electronic properties of surface elements were investigated by conducting XPS analysis (Fig. S16) on pure CdNCN synthesized using the Dronskowski reported method (Fig. S17) [10], as well as CdNCN-CdS-0.5, CdNCN-CdS-1, CdNCN-CdS-3, and CdS-15 samples. The XPS results reveal a significant abundance of C=N bonds in the initial four samples, while negligible amounts were detected in the CdS-15. Despite considerable electron transfer occurring between the $[NCN]^{2-}$ group and Cd atoms at the interface, there was no noticeable variation observed in the Cd 3d binding energy across all samples. However, a positive shift of 0.12 eV in the S 2p binding energy indicates spontaneous electron transfer from electron-rich S^{2-} to electron-deficient Cd^{2+}, which contributes to maintaining charge balance. Detailed analysis procedures can be found in Supplementary Material. Furthermore, through the utilization of in-situ XPS for monitoring the surface chemical state changes between the ground and excited states of the samples, it becomes possible to determine trends in electron transfer between substances. Fig. S18a reveals that both pre and post-illumination survey spectra of the samples exhibit stable peak positions and relative intensities, indicating a stable chemical composition of the catalyst under light irradiation. The high-resolution in-situ XPS analysis presented in Fig. 3 provides detailed insights into N 1s and S 2p in the CdNCN-CdS-1 sample. In the dark state, the binding energy peak of the Cd–C=N bond is observed at 397.56 eV in the N 1s peaks. Upon photoexcitation with 405 nm light, a negative shift of 0.18 eV is observed in this peak, confirming electron enrichment in CdNCN under photoexcitation conditions (Fig. 3a). Simultaneously, the S 2p peaks exhibit a positive shift of 0.12 eV under illumination, compared to the dark conditions (Fig. 3b). Additionally, during this process, it can be observed that the XPS peak positions of Cd 3d almost remain unchanged (Fig. S18b). This result illustrates a spontaneous electron transfer from the electron-rich S^{2-} to the electron-deficient Cd^{2+}, maintaining overall charge balance within the system. To determine the localization and delocalization of electrons at the transition structures between N–Cd–S, ELF calculations were employed. These calculations help visualize the electron clouds at the transition structures, providing insights into the distribution of electrons among the atoms [31,32]. In Fig. 3c, ELF values are depicted using a color scheme where yellow indicates high electron localization and blue signifies electron delocalization. The side-view ELF image of CdNCN-CdS shows localized electron clouds between N and Cd. At the N-Cd connection sites, the valence electron cloud of N atoms expands on the side where it connects to Cd atoms. This expansion results from the strong electron attraction of N atoms pulling the valence electrons from Cd, leading to a redistribution of electron clouds that confirms the tight binding between N and Cd atoms. Moreover, at the S-Cd connection, the electron cloud of S atoms also shifts towards Cd atoms, further illustrating the pathway of electron transfer through the N-Cd-S sites. The ELF values at the N-Cd connections are around 0.5 (Fig. 3c left), indicative of an efficient electron transfer pathway between these atoms [33,34]. By integrating the spectral information from in-situ and ex-situ XPS measurements with ELF analysis, a comprehensive electron transfer model for the S-Cd-[NCN] system is established (Fig. 3c right): Electrons spontaneously transfer from CdS through the N-Cd-S transition interface within the CdS-CdNCN structure towards CdNCN, irrespective of the material being in the ground or excited state.

Atomic force microscopy (AFM) in tapping mode was utilized to precisely characterize the microstructure of the CdNCN-CdS-1 sample (Fig. 3d and Figs. S19a–b). The AFM images revealed the presence of CdS nanoparticles, approximately 150 nm in diameter, distributed on the CdNCN nanosheets. Additionally, AFM-KPFM, which measures surface potentials with nanometer-scale resolution, was employed to visualize the surface photovoltage (SPV). This technique helped determine the direction of charge transfer of photo-generated electrons between CdNCN and CdS [35,36]. Under AM1.5G light illumination, 2D SPV testing revealed circular regions of high potential surrounded by areas of lower potential on the CdNCN nanosheets (Fig. 3e left), indicating significant electron accumulation on CdNCN. This phenomenon suggests that photo-generated electrons transferring through the Cd-N electron transfer channel to the surface of the CdNCN, creating a noticeable surface potential difference. The contact potential difference (ΔCPD) measured on the sample surface reflects the efficacy of hole-electron separation. During light irradiation, the ΔCPD at the CdNCN-CdS binding sites reached a maximum of 33.9 mV (Fig. 3e right), surpassing the ΔCPD of 23.8 mV observed under dark conditions (Figs. S19c–d). This higher ΔCPD signifies a strong driving force, attributed to the intense built-in electric field within the sample, facilitating effective photogenerated charge separation. Ultimately, KPFM measurements confirmed the nanoscale charge transfer trend between CdNCN and CdS (Fig. 3f). To study the excitation and decay of photogenerated carriers in CdNCN-CdS-1 and evaluate different energy level transitions and electron transfer phenomena, we used femtosecond transient absorption spectroscopy (fs-TAS) to assess the ultrafast carrier dynamics of the sample. The time-resolved behavior of the excited state in the CdNCN-CdS-1 sample is shown in Figs. S20a–c, including excited state absorption (ESA), ground state bleaching (GSB), and stimulated emission (SE) signals. Typically, the ESA signal arises from light absorption by excited-state electrons [37]. After pumping at 400 nm, CdNCN-CdS-1 exhibited an enhanced ESA signal over time, with the strongest ESA signal observed at 968 fs and remaining stable for a period, indicating that the sample had reached its optimal excitation level. Simultaneously, a negative ΔOD signal appeared at 463 fs, which corresponds to the GSB signal in fs-TAS. The appearance of the GSB signal is generally attributed to the depletion of ground-state molecules that absorb pump light due to the reduced number of ground-state molecules during photoexcitation [38]. Consequently, the GSB signal strengthens alongside the ESA signal and reaches its most negative value at 1.5 ps, after the ESA signal peaks. We further fitted the time-resolved data for the wavelengths representing ESA, GSB, and SE signals (Figs. S20d–f and Table S3) and obtained decay times of 5364.28 ps, 1270.93 ps, and 2490.71 ps, respectively. The GSB attenuation at 577 nm for CdNCN-CdS-1 exceeds the reported GSB attenuation value for CdS in the literature (393.38 ps), demonstrating the excellent electron-hole separation efficiency of CdS-CdNCN-1 [39]. The long decay times of the ESA and SE signals suggest that the photogenerated electron-hole pairs were successfully separated in the sample, thereby demonstrating that CdNCN-CdS-1 exhibits efficient carrier separation [40].

Steady-state photoluminescence spectroscopy was employed to conduct fluorescence emission tests on samples. As depicted in Fig. S21, with an increase in the proportion of CdNCN in the samples, there is a gradual blue-shift of the fluorescence emission peak accompanied by an enhancement in emission intensity. This phenomenon can be attributed to the enhanced ultraviolet absorption by the $[N=C=N]^{2-}$ moieties, which intensifies and shifts the fluorescence emission peaks [41,42]. As the content of $[NCN]^{2-}$ moieties decreases, CdNCN-CdS-3 and CdS-15 exhibit lower fluorescence emission intensities. Notably, CdNCN-CdS-1 shows a fluorescence emission intensity similar to that of CdNCN-CdS-3. This is attributed to the optimal ratio of CdNCN to CdS in CdNCN-CdS-1, which enhances its charge separation capability and suppresses the fluorescence emission of the $[NCN]^{2-}$ moieties [43,44]. The electrochemical properties were further evaluated through electrochemical impedance spectroscopy (EIS). In the Nyquist plot, the CdNCN-CdS-1 sample demonstrates the lowest resistance (Fig. S22), indicating an enhanced ability for charge transfer. Moreover, transient photocurrent response tests confirmed that that the CdNCN-CdS-1 sample displays optimal performance in terms of photoexcited electron behavior (Fig. S23). These assessments, combined with the EIS and PL results, provide additional evidence supporting efficient separation and transfer of photogenerated electrons at the CdNCN-CdS interface. Due to the strong charge separation and transfer ability at the CdNCN/CdS interface, the CdNCN-CdS samples exhibit exceptional hydrogen evolution activity. Notably, the optimal CdNCN-CdS-1 sample, without any

cocatalysts, achieves a groundbreaking photocatalytic hydrogen evolution efficiency of 14.7 mmol g^{-1} h^{-1} ($\lambda > 420$ nm). This efficiency surpasses those of the CdNCN-CdS-0.5, CdNCN-CdS-3, and CdS-15 samples by factors of 2.37, 3.45, and 7.56 respectively, setting a new benchmark for CdS-based semiconductor heterostructures (Fig. 3g and h) [45–65]. Furthermore, the CdNCN-CdS-1 sample maintained robust hydrogen evolution performance even after five cycles, demonstrating its durability (Fig. S24). We supplemented our analysis with XRD, SEM of the material and ICP test data of the solution after the reaction (Fig. S25 and Table S2). The XRD peaks of the CdNCN-CdS-1 sample remained almost unchanged, indicating that the sample maintained good stability even after prolonged reactions. In SEM images, CdNCN exhibited partial agglomeration, which is due to the inevitable aggregation of nanosheets after prolonged hydrogen evolution reactions. Under illumination with 400 nm light, the apparent quantum efficiency (AQY) of the CdNCN-CdS-1 sample reaches an impressive 20.5 %, as shown in Fig. S26 and Tables S4–6, The exceptional photocatalytic performance can be attributed to the unique crystal and two-dimensional structure of CdNCN, which effectively reduces carrier migration distances and facilitates rapid electron transfer.

The photoresponse of CdNCN in Fig. 4a exhibits a remarkable step-like behavior. In the ultraviolet–visible (UV–Vis) region spanning from 300 to 550 nm, CdNCN demonstrates a strong and particularly intense response to ultraviolet light, especially below 300 nm. This enhanced response can be ascribed to the conjugation effect arising from unsaturated N=C=N groups. Additionally, Fig. 4b and Fig. S27 presents the UV–Vis diffuse reflectance spectroscopy (UV–Vis DRS) of all samples prepared with varying molar ratios of $CdCl_2$ to thiourea. In the CdS-15 sample, the absorption edge is positioned around 600 nm. However, as the molar ratio of thiourea decreases, leading to an increased proportion of CdNCN in the composite, the absorption edge of the catalyst shifts to shorter wavelengths, nearing 500 nm. This shift indicates a change in the optical properties of the composite as the content of CdNCN increases, which consequently affects its overall light absorption and photocatalytic performance.

The UV–Vis DRS was employed to analyze the bandgap structure of

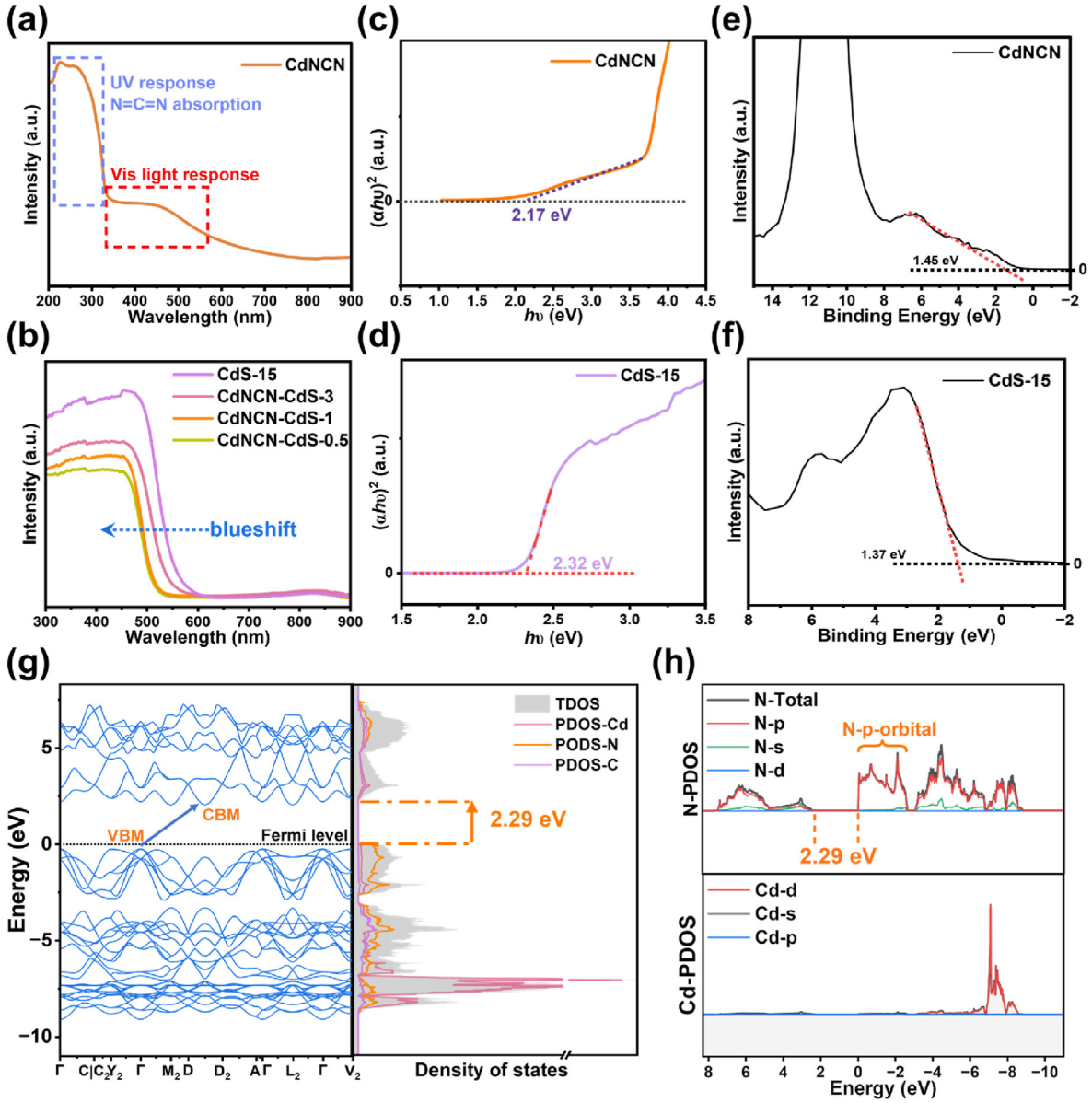

Fig. 4. UV–Vis diffuse reflectance spectroscopy (DRS) test: (a) CdNCN, (b) samples obtained at different $CdCl_2$ to thiourea molar ratios; Tauc plot of different samples: (c) CdNCN; (d) CdS-15; VB-XPS test of different samples: (e) CdNCN, (f) CdS-15; (g–h) Band calculation and TDOS calculation of CdNCN semiconductor (g) and PDOS calculation (h).

CdS-15 and CdNCN using the Tauc formula. Consequently, both samples exhibit bandgaps of 2.32 eV and 2.17 eV, respectively (Fig. 4c and d). Further analysis using valence-band X-ray photoemission spectroscopy (VB-XPS) identified the VB edges relative to the Fermi level, with CdNCN at 1.45 eV (vs E_F) and CdS-15 at 1.37 eV (vs E_F). By converting these values to the normal hydrogen electrode (NHE) scale using the formula $E_{VB,\ NHE}=\varphi+E_{VB\text{-}XPS}-4.44$ [66] (where φ=4.2 eV, the instrument work function), followed by conversion to the reversible hydrogen electrode (RHE) scale, the VB potential (E_{VB}) of CdNCN and CdS are determined to be 1.62 V and 1.54 V (vs RHE), respectively (Fig. 4e and f). The conduction band potential (E_{CB}) positions were determined by calculating using the formula $E_{CB}=E_g-E_{VB}$, resulting in −0.55V for CdNCN and −0.78V for CdS-15 (Table S7). Moreover, Mott-Schottky (M − S) tests revealed flat band potential (E_{fb}) of −0.50 V and −0.63 V for the CdNCN and CdS-15 samples, respectively, as shown in Figs. S28a–b [67]. Given that the E_{CB} is typically approximately 0.1 V more negative than the E_{fb} [68], the E_{CB} values are adjusted to -0.60 V for CdNCN and -0.73 V (vs RHE) for CdS-15. Ultimately, the VB potential for CdNCN and CdS-15 are determined to be 1.57 V and 1.59 V (vs RHE), respectively (Table S8). To investigate the detailed bandgap structure of CdNCN, density functional theory (DFT) calculations were employed to derive both the band structure and the density of states - projected density of states (TDOS-PDOS). This approach helped delineate the excitation mechanism of CdNCN. It is important to note that standard DFT calculations often underestimate band structures due to incomplete descriptions of electron-electron interactions. To address this, an adjustment for electron Coulomb force (DFT+U) was applied [69]. The crystal structure used for band structure and density of states calculations is illustrated in Fig. S29. In these calculations, the bandgap of CdNCN is measured to be 2.29 eV. Additionally, the valence band maximum (VBM) and conduction band minimum (CBM) are determined to be located at the Γ and D-D_2 wave vectors, respectively. The VBM and CBM located at different wave vectors dictates that electronic transitions require not only energy excitation but also phonon participation to change the electronic momentum and ultimately reach the conduction band minimum. This characteristic confirms that CdNCN belongs to a typical indirect bandgap semiconductor (Fig. 4g). Further identified the atomic orbital positions contributing to the VBM in CdNCN through partial density of states (PDOS). The N-PDOS analysis reveals that at the VBM, the energy near 0 eV is predominantly associated with the p orbital electrons of nitrogen (Fig. 4h). This finding implies that during photoexcitation, transitions of nitrogen's p orbital electrons from the VBM to the CBM play a crucial role in the photocatalytic hydrogen evolution reaction.

The surface work function reflects the minimum e to its surface vacuum layer. The magnitude of this work function indicates differences in the electron work functions between materials, thereby revealing the potential for electron transfer [15]. As depicted in Fig. 5a and b, the work function values of the CdS-(002) crystal plane and the CdNCN-(002) crystal plane samples are determined to be 5.13 eV and 8.28 eV, respectively. It is noteworthy that the CdNCN-(002) crystal plane exhibits two distinct work function values corresponding to its top and bottom surfaces, indicating the presence of two different electron emission conditions. This disparity in work function primarily arises from the heterogeneity in surface atomic arrangements. Generally, the presence of an outwardly directed surface polarization electric field perpendicular to the surface leads to an increase in the system's work function. Due to the attractive capability of $[NCN]^{2-}$ moieties towards external charges, a polarization electric field along the (002)-$[NCN]^{2-}$ surface towards the vacuum layer is generated, ultimately resulting the difference in work function [70]. When CdS and CdNCN come into contact, electrons

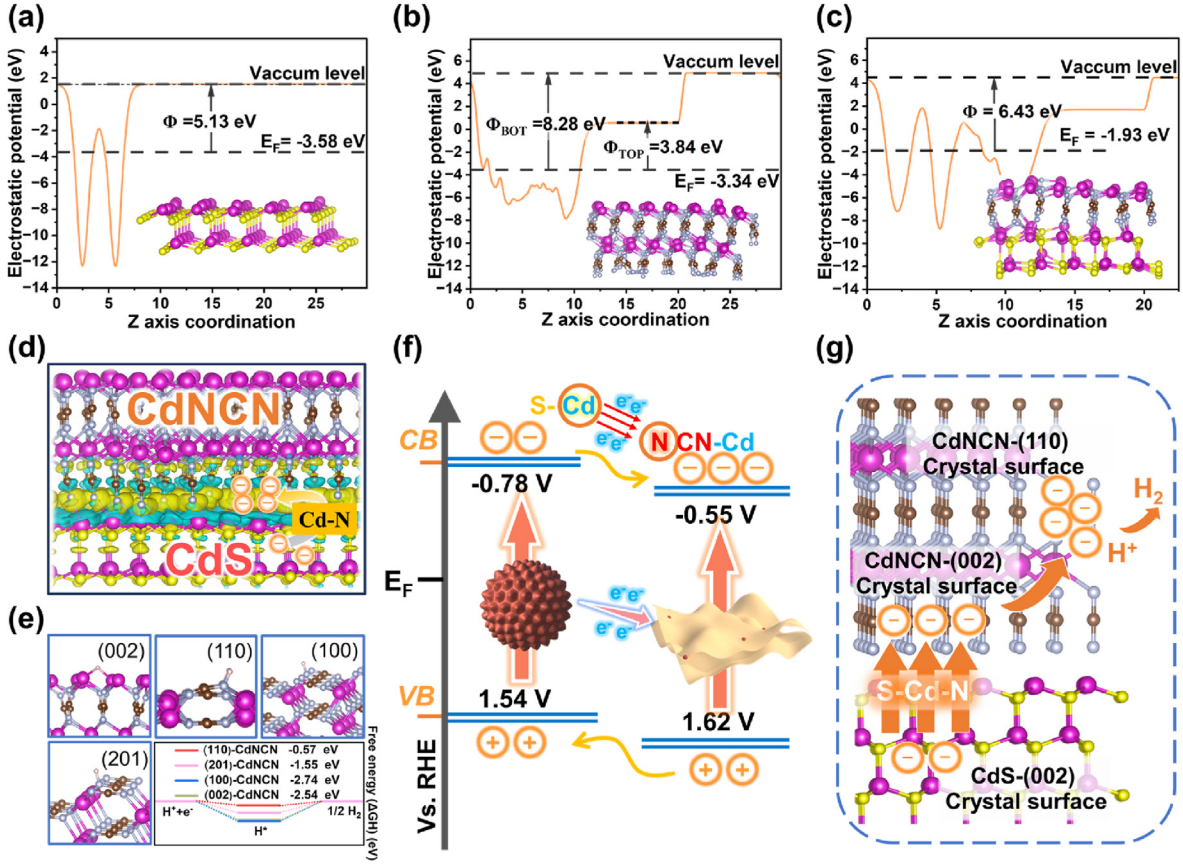

Fig. 5. Work function calculations for different components: (a) CdS, (b) CdNCN, and (c) CdS- CdNCN; (d) Differential charge density between CdNCN and CdS; (e) Calculation of Gibbs free energy of H adsorption (ΔG_H) on different crystal facets of CdNCN; (f) Band gap structure analysis of CdS-CdNCN; (g) Schematic diagram of charge transfer in CdS-CdNCN(002)-CdNCN(110)-H_2 system.

transfer from from the material with the lower work function (CdS) to the material with the higher work function (CdNCN) to balance the potential difference across the interface. As depicted in Fig. 5c, the resulting work function of the CdNCN-CdS heterojunction is calculated to be 6.43 eV. Fig. 5d and Fig. S30 illustrates this electron transfer, which is confirmed by the electron gain-loss layer depicted in the differential charge density plot for the CdNCN-CdS interface. Considering the influence of different crystal facets on the adsorption capacity of hydrogen atoms, we evaluated the adsorption free energy of hydrogen atoms on various crystal facets of CdNCN. The optimal adsorption sites for hydrogen atoms on the (002), (110), (100), and (201) crystal facets are displayed in Fig. 5e, with adsorption free energies of -2.54 eV, -0.57 eV, -2.74 eV and -1.55 eV, respectively. In the process of photocatalytic hydrogen evolution, the affinity between hydrogen atoms and surface sites plays a crucial role in determining the overall reaction progression; excessive adsorption can prevent the release of hydrogen atoms post-H_2 formation, while excessively strong desorption can inhibit hydrogen participation in surface redox reactions. Therefore, a Gibbs free energy of adsorption close to 0 eV is most favorable for the hydrogen evolution process [71]. Based on this fact, it is evident that the N-(110) site emerged as the most effective active site for photocatalytic hydrogen evolution reactions, providing a balanced adsorption property conducive to effective hydrogen evolution. At the same time, the hydrogen adsorption free energy of CdS was also calculated and the values are shown in Fig. S31. To further determine the electron flow within different crystal planes, we simulated the band structures of various planes of CdNCN. As shown in Figs. S32–S33, due to the difference in the valence band and conduction band positions on different crystal planes, electrons will be directionally transferred from the (002) plane to the (110) plane [72].

Based on experimental and theoretical findings, we propose the mechanism for electron transfer at the CdS-CdNCN interface and elucidate the role of CdNCN in photocatalytic reactions. Initially, due to the presence of a polarizing electric field, CdNCN exhibits a significantly higher work function (Φ) compared to CdS. When CdNCN and CdS come into close contact, as depicted in Fig. 5f, electrons migrate from CdS to CdNCN to equilibrate the work function disparity. Simultaneously, owing to differences in electronegativity, N atoms within the NCN-Cd-S atomic-level heterostructure exhibit a pronounced attraction towards the valence electron cloud of Cd atoms, there fostering rapid electron transfer. Moreover, the ELF calculation results demonstrate the formation of an electron transfer pathway of N-Cd-S between CdNCN and CdS. During photocatalysis, the strong electronic transport effect driven by Cd-N interactions accelerates the transfer of photogenerated electrons to the surface of CdNCN. As shown in Fig. 5g, these transferred electrons encounter spatial hindrance and atomic affinity differences caused by diverse atomic arrangements, guiding their migration from the (002) crystal plane to the (110) crystal plane. The (110) plane, which exhibits optimal hydrogen atom adsorption energy, facilitates the participation of electrons in the hydrogen evolution reaction, thereby enhancing the photocatalytic efficiency of the system.

3. Conclusion

By leveraging the concentration gradient of thiourea in a spatiotemporal manner, we achieve the controlled preparation of CdNCN-CdS composite catalysts featuring atomic-level N–Cd–S heterostructures. The optimal CdNCN-CdS sample without the need for additional co-catalysts, exhibits an unprecedented photocatalytic hydrogen evolution rate among CdS-based photocatalysts. This exceptional performance is primarily attributed to the tight integration of heterostructures at the N–Cd–S transition sites at the CdNCN-CdS interface, reducing electron transfer resistance at the heterojunction; and the presence of electronegative nitrogen in the N–Cd–S transition structure, accelerating charge transfer from CdS to CdNCN and enhancing the separation of photogenerated electron-hole pairs. This work opens new avenues for the utilization of thiourea molecules, establishes a charge transfer model based on atomic-level homologous heterostructures, and offers new possibilities for constructing novel semiconductor systems.

4. Experimental section

4.1. Preparation of CdNCN-CdS composite catalyst

The thoroughly mixed solution consisted of 60 mL of 3 mmol $CdCl_2$, with magnetic stirring employed. Subsequently, the pH was adjusted to 11 using ammonia solution (Tianjin Damao, 28%). The reaction mixture was heated in an oil bath at a temperature of 60 °C until it reached this temperature. Then, varying amounts of thiourea (Aladdin, AR 99%), namely 1.5 mmol, 3 mmol, 9 mmol, or 45 mmol were added accordingly. The reaction was carried out in the 60 °C for 3 h to obtain samples with molar ratios of $CdCl_2$ to thiourea as 1:0.5, 1:1, 1:3, and 1:15 respectively. These samples are denoted as CdNCN-CdS-0.5, CdNCN-CdS-1, CdNCN-CdS-3, and CdS-15.

4.2. Photocatalytic hydrogen production performance test

In the standard photocatalytic hydrogen evolution process, 10 mg of the catalyst sample was added to a 100 mL solution containing 0.35 mol L^{-1} Na_2S and 0.25 mol L^{-1} Na_2SO_3. The suspension was transferred to a quartz-sealed container that could be irradiated from the top. To remove air from the system, nitrogen gas was bubbled into the reaction vessel for 30 min. A xenon lamp with an intensity of 300 W served as the light source, while visible light was obtained by employing a cutoff filter at 420 nm to eliminate ultraviolet radiation. Gas chromatography (GC-7900) was employed to analyze the extracted gas from the reactor every hour for calculating the photocatalytic hydrogen evolution efficiency.

CRediT authorship contribution statement

Taiyu Huang: Writing – original draft, Methodology, Investigation, Data curation. **Zimo Huang:** Supervision, Investigation, Data curation. **Xixian Yang:** Validation, Resources, Formal analysis. **Siyuan Yang:** Methodology, Formal analysis. **Qiongzhi Gao:** Validation, Resources. **Xin Cai:** Supervision, Investigation. **Yingju Liu:** Supervision, Formal analysis. **Yueping Fang:** Visualization, Resources, Funding acquisition, Formal analysis. **Shanqing Zhang:** Supervision, Methodology, Investigation. **Shengsen Zhang:** Writing – review & editing, Resources, Project administration, Investigation, Funding acquisition, Conceptualization.

Acknowledgements

This work was financially supported by the National Natural Science Foundation of China (Nos. 22078118, 22274059 and 42277219) and the Natural Science Foundation of Guangdong Province, China (Nos. 2023A1515010740 and 2023A1515030131).

Appendix A. Supplementary data

Supplementary data to this article can be found online at https://doi.org/10.1016/j.apmate.2024.100242.

References

[1] T. Takata, J. Jiang, Y. Sakata, M. Nakabayashi, N. Shibata, V. Nandal, K. Seki, T. Hisatomi, K. Domen, Photocatalytic water splitting with a quantum efficiency of almost unity, Nature 581 (2020) 411–414.
[2] M.V. Pavliuk, S. Wrede, A. Liu, A. Brnovic, S. Wang, M. Axelsson, H. Tian, Preparation, characterization, evaluation and mechanistic study of organic polymer nano-photocatalysts for solar fuel production, Chem. Soc. Rev. 51 (2022) 6909–6935.
[3] L. Chen, M.A. Maigbay, M. Li, X. Qiu, Synthesis and modification strategies of g-C_3N_4 nanosheets for photocatalytic applications, Adv. Powder Mater. 3 (2024) 100150.

[4] S. Li, M. Cai, Y. Liu, C. Wang, R. Yan, X. Chen, Constructing $Cd_{0.5}Zn_{0.5}S/Bi_2WO_6$ S-scheme heterojunction for boosted photocatalytic antibiotic oxidation and Cr(VI) reduction, Adv. Powder Mater. 2 (2023) 100073.
[5] C. Xu, P.R. Anusuyadevi, C. Aymonier, R. Luque, S. Marre, Nanostructured materials for photocatalysis, Chem. Soc. Rev. 48 (2019) 3868–3902.
[6] C.Z. Ning, L. Dou, P. Yang, Bandgap engineering in semiconductor alloy nanomaterials with widely tunable compositions, Nat. Rev. Mater. 2 (2017) 17070.
[7] R. Woods-Robinson, Y. Han, H. Zhang, T. Ablekim, I. Khan, K.A. Persson, A. Zakutayev, Wide band gap chalcogenide semiconductors, Chem. Rev. 120 (2020) 4007–4055.
[8] B. Jia, D. Sun, W. Zhao, F. Xu, F. Huang, Controllable conversion of CdNCN nanoparticles into various chalcogenide nanostructures for photo-driven applications, Chem. Eur J. 26 (2020) 7955–7960.
[9] X. Qiao, K. Chen, A.J. Corkett, D. Mroz, X. Huang, R. Wang, R. Nelson, R. Dronskowski, Synthesis, crystal structure, symmetry relationships, and electronic structure of bismuth carbodiimide $Bi_2(NCN)_3$ and its ammonia adduct $Bi_2(NCN)_3{\bullet}NH_3$, Inorg. Chem. 60 (2021) 12664–12670.
[10] X. Qiao, D. Mroz, A.J. Corkett, T. Bisswanger, R. Dronskowski, Metathesis and redetermination of the crystal structure of cadmium carbodiimide, CdNCN, Z. Anorg. Allg. Chem. 647 (2021) 496–499.
[11] J. Li, R. Wang, P. Guo, X. Liu, Y. Hu, Z. Xu, Y. Liu, L. Cao, J. Huang, K. Kajiyoshi, Realizing fast charge diffusion in oriented iron carbodiimide structure for high-rate sodium-ion storage performance, ACS Nano 15 (2021) 6410–6419.
[12] L. Zhang, J. Zhang, H. Yu, J. Yu, Emerging S-scheme photocatalyst, Adv. Mater. 34 (2022) 2107668.
[13] W. Shang, W. Liu, X. Cai, J. Hu, J. Guo, C. Xin, Y. Li, N. Zhang, N. Wang, C. Hao, Y. Shi, Insights into atomically dispersed reactive centers on g-C_3N_4 photocatalysts for water splitting, Adv. Powder Mater. 2 (2023) 100094.
[14] G. Zhao, W. Ma, X. Wang, Y. Xing, S. Hao, X. Xu, Self-water-absorption-type two-dimensional composite photocatalyst with high-efficiency water absorption and overall water-splitting performance, Adv. Powder Mater. 1 (2022) 100008.
[15] T.Y. Huang, Z. Yang, S.Y. Yang, Z.H. Dai, Y.J. Liu, J.H. Liao, G.Y. Zhong, Z.J. Xie, Y.P. Fang, S.S. Zhang, Construction of 2D/2D $Ti_3C_2T_x$ MXene/CdS heterojunction with photothermal effect for efficient photocatalytic hydrogen production, J. Mater. Sci. Technol. 171 (2024) 1–9.
[16] T. Zhang, F. Meng, Y. Cheng, N. Dewangan, G.W. Ho, S. Kawi, Z-scheme transition metal bridge of Co_9S_8/Cd/CdS tubular heterostructure for enhanced photocatalytic hydrogen evolution, Appl. Catal. B Environ. 286 (2021) 119853.
[17] X. Ruan, D. Meng, C. Huang, M. Xu, D. Jiao, H. Cheng, Y. Cui, Z. Li, K. Ba, T. Xie, L. Zhang, W. Zhang, J. Leng, S. Jin, S.K. Ravi, Z. Jiang, W. Zheng, X. Cui, J. Yu, Artificial photosynthetic system with spatial dual reduction site enabling enhanced solar hydrogen production, Adv. Mater. 36 (2024) 2309199.
[18] J. Zheng, K. Lebedev, S. Wu, C. Huang, T.S. Wu, Y. Li, P.L. Ho, Y.L. Soo, A. Kirkland, S.C.E. Tsang, High loading of transition metal single atoms on chalcogenide catalysts, J. Am. Chem. Soc. 143 (2021) 7979–7990.
[19] J.A. García-Valenzuela, Simple thiourea hydrolysis or intermediate complex mechanism? taking up the formation of metal sulfides from metal–thiourea alkaline solutions, Comments Mod. Chem. 37 (2017) 99–115.
[20] M. Thambidurai, N. Murugan, N. Muthukumarasamy, S. Agilan, S. Vasantha, R. Balasundaraprabhu, Influence of the Cd/S molar ratio on the optical and structural properties of nanocrystalline CdS thin films, J. Mater. Sci. Technol. 26 (2010) 193–199.
[21] R. Gaur, P. Jeevanandam, Effect of anions on the morphology of CdS nanoparticles prepared via thermal decomposition of different cadmium thiourea complexes in a solvent and in the solid state, New J. Chem. 39 (2015) 9442–9453.
[22] J.A. García-Valenzuela, Simple thiourea hydrolysis or intermediate complex mechanism? taking up the formation of metal sulfides from metal–thiourea alkaline solutions, Comments Mod. Chem. 37 (2016) 99–115.
[23] M. Freda, A. Piluso, A. Santucci, P. Sassi, Transmittance fourier transform infrared spectra of liquid water in the whole mid-infrared region: temperature dependence and structural analysis, Appl. Spectrosc. 59 (2005) 1155–1159.
[24] C.B. Dai, H.Y. Zhang, R.D. Li, H.F. Zou, Synthesis and characterization of thiourea, Pol. J. Chem. Technol. 21 (2019) 35–39.
[25] Z. Kartal, O. Sahin, Synthesis, spectroscopic, thermal, crystal structure properties and characterization of new hofmann-type-like clathrates with 4-aminopyridine and water, Turk. J. Chem. 45 (2021) 616–633.
[26] C.W. Ding, M.J. Zhang, N. Ma, Research progress in the synthetic methods of thioureas, Chinese J. Org. Chem. 30 (2010) 173–180.
[27] D. Williams, Frequency assignments in infra-red spectrum of water, Nature 210 (1966) 194–195.
[28] Y. Tao, W. Zou, D. Sethio, N. Verma, Y. Qiu, C. Tian, D. Cremer, E. Kraka, In situ measure of intrinsic bond strength in crystalline structures: local vibrational mode theory for periodic systems, J. Chem. Theory. Comput. 15 (2019) 1761–1776.
[29] X. Tang, H. Xiang, X. Liu, M. Speldrich, R. Dronskowski, A ferromagnetic carbodiimide: $Cr_2(NCN)_3$, Angew. Chem. Int. Ed. Engl. 49 (2010) 4738–4742.
[30] T.D. Boyko, R.J. Green, R. Dronskowski, A. Moewes, Electronic band gap reduction in manganese carbodiimide: MnNCN, J. Phys. Chem. C 117 (2013) 12754–12761.
[31] L. Meng, Y. Wang, L. Zhang, S. Du, R. Wu, L. Li, Y. Zhang, G. Li, H. Zhou, W.A. Hofer, H.J. Gao, Buckled silicene formation on Ir(111), Nano Lett. 13 (2013) 685–690.
[32] D. Han, J. Wang, L. Agosta, Z. Zang, B. Zhao, L. Kong, H. Lu, I. Mosquera-Lois, V. Carnevali, J. Dong, J. Zhou, H. Ji, L. Pfeifer, S.M. Zakeeruddin, Y. Yang, B. Wu, U. Rothlisberger, X. Yang, M. Grätzel, N. Wang, Tautomeric mixture coordination enables efficient lead-free perovskite LEDs, Nature 622 (2023) 493–498.
[33] A. Savin, O. Jepsen, J. Flad, O.K. Andersen, H. Preuss, H.G. von Schnering, Electron localization in solid-state structures of the elements: the diamond structure, Angew. Chem. Int. Edit. 31 (2003) 187–188.
[34] A.D. Becke, K.E. Edgecombe, A simple measure of electron localization in atomic and molecular systems, J. Chem. Phys. 92 (1990) 5397–5403.
[35] B. Xia, B. He, J. Zhang, L. Li, Y. Zhang, J. Yu, J. Ran, S.Z. Qiao, $TiO_2/FePS_3$ S-scheme heterojunction for greatly raised photocatalytic hydrogen evolution, Adv. Energy Mater. 12 (2022) 2201449.
[36] J. Barnett, L. Wehmeier, A. Heßler, M. Lewin, J. Pries, M. Wuttig, J.M. Klopf, S.C. Kehr, L.M. Eng, T. Taubner, Far-infrared near-field optical imaging and kelvin probe force microscopy of laser-crystallized and amorphized phase change material $Ge_3Sb_2Te_6$, Nano Lett. 21 (2021) 9012–9020.
[37] T. Zhang, T. Li, M. Gao, W. Lu, Z. Chen, W.L. Ong, A.S.W. Wong, L. Yang, S. Kawi, G.W. Ho, Ligand mediated assembly of CdS colloids in 3D porous metal–organic framework derived scaffold with multi-sites heterojunctions for efficient CO_2 photoreduction, Adv. Energy Mater. 14 (2024) 2400388.
[38] Y. Tamai, Y. Murata, S.I. Natsuda, Y. Sakamoto, How to interpret transient absorption data?: an overview of case studies for application to organic solar cells, Adv. Energy Mater. 14 (2024) 2301890.
[39] Y. Zhang, D. Ma, S. Jiang, J. Zhang, S. Song, Optimization of d-p band centers as efficient active sites for solar energy conversion into H_2 by tuning surface atomic arrangement, Appl. Catal., B: Environment and Energy 359 (2024) 124500.
[40] C. Bie, B. Zhu, L. Wang, H. Yu, C. Jiang, T. Chen, J. Yu, A bifunctional CdS/MoO_2/MoS_2 catalyst enhances photocatalytic H_2 evolution and pyruvic acid synthesis, Angew. Chem. Int. Edit. 61 (2022) e202212045.
[41] R. Shen, C. Qin, L. Hao, X. Li, P. Zhang, X. Li, Realizing photocatalytic overall water splitting by modulating the thickness-induced reaction energy barrier of fluorenone-based covalent organic frameworks, Adv. Mater. 35 (2023) 2305397.
[42] X. Sun, M. Song, F. Liu, H. Peng, T. Zhao, S.F. Yin, P. Chen, Interfacial chemical bond regulating the electronic coupling of $ZnIn_2S_{4-x}$-WO_{3-x} for enhancing the photocatalytic pollution degradation coupled with hydrogen evolution, Appl. Catal. B Environ. 342 (2024) 123436.
[43] R. Shen, X. Li, C. Qin, P. Zhang, X. Li, Efficient photocatalytic hydrogen evolution by modulating excitonic effects in Ni-intercalated covalent organic frameworks, Adv. Energy Mater. 13 (2023) 2203695.
[44] Y. Zhang, Q. Cao, A. Meng, X. Wu, Y. Xiao, C. Su, Q. Zhang, Molecular heptazine–triazine junction over carbon nitride frameworks for artificial photosynthesis of hydrogen peroxide, Adv. Mater. (2023) 2306831.
[45] X. Jia, M. Tahir, L. Pan, Z.F. Huang, X. Zhang, L. Wang, J.J. Zou, Direct Z-scheme composite of CdS and oxygen-defected $CdWO_4$: an efficient visible-light-driven photocatalyst for hydrogen evolution, Appl. Catal. B Environ. 198 (2016) 154–161.
[46] J. Du, H. Wang, M. Yang, K. Li, L. Zhao, G. Zhao, S. Li, X. Gu, Y. Zhou, L. Wang, Y. Gao, W. Wang, D.J. Kang, Pyramid-like CdS nanoparticles grown on porous TiO_2 monolith: an advanced photocatalyst for H_2 production, Electrochim. Acta 250 (2017) 99–107.
[47] S. Li, L. Wang, S. Liu, B. Xu, N. Xiao, Y. Gao, W. Song, L. Ge, J. Liu, In situ synthesis of strongly coupled Co_2P-CdS nanohybrids: an effective strategy to regulate photocatalytic hydrogen evolution activity, ACS Sustain. Chem. Eng. 6 (2018) 9940–9950.
[48] R.K. Chava, N. Son, Y.S. Kim, M. Kang, Integration of perovskite type Bi_2MoO_6 nanosheets onto one dimensional CdS: a type-II heterostructured photocatalytic system for efficient charge separation in the hydrogen evolution reaction, Inorg. Chem. Front. 7 (2020) 2818–2832.
[49] J. Ran, H. Zhang, S. Fu, M. Jaroniec, J. Shan, B. Xia, Y. Qu, J. Qu, S. Chen, L. Song, J.M. Cairney, L. Jing, S.Z. Qiao, $NiPS_3$ ultrathin nanosheets as versatile platform advancing highly active photocatalytic H_2 production, Nat. Commun. 13 (2022) 4600.
[50] Y. Wu, Y. Qu, C. Su, X. Yang, Y. Yang, Y. Zhang, W. Huang, Enhanced photoinduced carrier separation in Fe-MOF-525/CdS for photocatalytic hydrogen evolution: improved catalytic dynamics with specific active sites, Inorg. Chem. 62 (2023) 21290–21298.
[51] Z. Chen, D. Li, C. Chen, Urchin-like TiO_2/CdS nanoparticles forming an S-scheme heterojunction for photocatalytic hydrogen production and CO_2 reduction, ACS Appl. Nano Mater. 6 (2023) 21897–21908.
[52] H. Wu, L. Zhao, X. He, H. Chen, W. Fang, X. Du, W. Li, D. Wang, Boosted charge carrier concentration via luminescent quenching of photoexcited electrons in CdS/FI S-scheme heterostructures for efficient photocatalytic hydrogen production, J. Clean. Prod. 425 (2023) 138921.
[53] L. Li, J. Luo, L. Chen, J. Shi, Photocorrosion-resistant $ZnCo2S_4$/CdS Z-scheme heterojunction for efficient Co-production of aromatic aldehydes and hydrogen, ACS Sustain. Chem. Eng. 11 (2023) 16703–16712.
[54] H. Hu, Y. He, H. Yu, D. Li, M. Sun, Y. Feng, C. Zhang, H. Chen, C. Deng, Constructing a noble-metal-free 0D/2D CdS/SnS_2 heterojunction for efficient visible-light-driven photocatalytic pollutant degradation and hydrogen generation, Nanotechnology 34 (2023) 505712.
[55] P. Hao, Y. Cao, X. Ning, R. Chen, J. Xie, J. Hu, Z. Lu, A. Hao, Rational design of CdS/BiOCl S-scheme heterojunction for effective boosting piezocatalytic H_2 evolution and pollutants degradation performances, J. Colloid Interf. Sci. 639 (2023) 343–354.
[56] F. Dong, L. Qin, T. Zhang, X. Li, S.Z. Kang, A novel pathway toward efficient improvement of the photocatalytic activity and stability of CdS-based photocatalyst for light driven H_2 evolution: the synergistic effect between CdS and $SrWO_4$, Int. J. Hydrogen Energ. 48 (2023) 13877–13889.
[57] A. Jiang, H. Guo, S. Yu, F. Zhang, T. Shuai, Y. Ke, P. Yang, Y. Zhou, Dual charge-accepting engineering modified $AgIn_5S_8$/CdS quantum dots for efficient

photocatalytic hydrogen evolution overall H_2S splitting, Appl. Catal. B Environ. 332 (2023) 122747.
[58] M. Shoaib, M.Y. Naz, S. Shukrullah, M.A. Munir, M. Irfan, S. Rahman, A.A.J. Ghanim, Dual S-Scheme heterojunction CdS/TiO_2/g-C_3N_4 photocatalyst for hydrogen production and dye degradation applications, ACS Omeg 8 (2023) 43139–43150.
[59] N. Jin, Y. Sun, W. Shi, P. Wang, Y. Nagaoka, T. Cai, R. Wu, L. Dube, H.N. Nyiera, Y. Liu, T. Mani, X. Wang, J. Zhao, O. Chen, Type-I CdS/ZnS core/shell quantum dot-gold heterostructural nanocrystals for enhanced photocatalytic hydrogen generation, J. Am. Chem. Soc. 145 (2023) 21886–21896.
[60] L. Shiuan Ng, T. Raja Mogan, J.K. Lee, H. Li, C.L. Ken Lee, H. Kwee Lee, Surface-degenerate semiconductor photocatalysis for efficient water splitting without sacrificial agents via a reticular chemistry approach, Angew. Chem. Int. Edit. 62 (2023) e202313695.
[61] G. Sun, Z. Tai, F. Li, Q. Ye, T. Wang, Z. Fang, L. Jia, W. Liu, H. Wang, Construction of $ZnIn_2S_4$/CdS/PdS S-Scheme heterostructure for efficient photocatalytic H_2 production, Small 19 (2023) 2207758.
[62] X. Luan, Z. Yu, J. Zi, F. Gao, Z. Lian, Photogenerated defect-transit dual S-scheme charge separation for highly efficient hydrogen production, Adv. Funct. Mater. 33 (2023) 2304259.
[63] L. Yang, T. Gao, S. Yuan, Y. Dong, Y. Chen, X. Wang, C. Chen, L. Tang, T. Ohno, Spatial charge separated two-dimensional/two-dimensional Cu-In_2S_3/CdS heterojunction for boosting photocatalytic hydrogen production, J. Colloid Interf. Sci. 652 (2023) 1503–1511.
[64] P. Bai, L. Junyu, S. Wang, H. Tong, W. Du, Z. Chai, Enhanced interfacial charge transfer by oxygen vacancies in ZnCdS/NiCo-LDH heterojunction for efficient H_2 evolution, Appl. Surf. Sci. 643 (2024) 158715.
[65] M. Yuan, J. Suriyaprakash, L. Shan, H. Xu, X. Li, H. Wu, G. Ding, Z. Shi, L. Dong, F.M. Zhang, Carrier confinement activated explicit solvent dynamic of CdS/$BiVO_4$/H_2O and optimized photocatalytic hydrogen evolution performances, J. Colloid Interf. Sci. 658 (2024) 571–583.
[66] X. Li, B. Kang, F. Dong, Z. Zhang, X. Luo, L. Han, J. Huang, Z. Feng, Z. Chen, J. Xu, B. Peng, Z.L. Wang, Enhanced photocatalytic degradation and H_2/H_2O_2 production performance of S-pCN/$WO_{2.72}$ S-scheme heterojunction with appropriate surface oxygen vacancies, Nano Energy 81 (2021) 105671.
[67] W. Lin, F. Lin, J. Lin, Z. Xiao, D. Yuan, Y. Wang, Efficient photocatalytic CO_2 reduction in ellagic acid–based covalent organic frameworks, J. Am. Chem. Soc. 146 (2024) 16229–16236.
[68] Z. Yang, M. Li, S.B. Chen, S.Y. Yang, F. Peng, J.H. Liao, Y.P. Fang, S.Q. Zhang, S.S. Zhang, Cocatalyst engineering with robust tunable carbon-encapsulated Mo-rich Mo/Mo_2C heterostructure nanoparticle for efficient photocatalytic hydrogen evolution, Adv. Funct. Mater. 33 (2023) 2212746.
[69] K.F. Mak, C. Lee, J. Hone, J. Shan, T.F. Heinz, Atomically thin MoS_2: a new direct-gap semiconductor, Phys. Rev. Lett. 105 (2010) 136805.
[70] Z.F. Hou, Z.Z. Zhu, M.C. Huang, R.B. Huang, L.S. Zheng, Work function change of Ag, Au, K adsorbed on W(001) surface as a function of external electric field, Acta Phys. Sinic 51 (2002) 1591–1595.
[71] Z. Yang, T. Huang, M. Li, X. Wang, X. Zhou, S. Yang, Q. Gao, X. Cai, Y. Liu, Y. Fang, Y. Wang, S. Zhang, S. Zhang, Unveiling the synergistic role of frustrated lewis pairs in carbon-encapsulated Ni/NiO_x photothermal cocatalyst for enhanced photocatalytic hydrogen production, Adv. Mater. 36 (2024) 2313513.
[72] Z. Luo, X. Ye, S. Zhang, S. Xue, C. Yang, Y. Hou, W. Xing, R. Yu, J. Sun, Z. Yu, X. Wang, Unveiling the charge transfer dynamics steered by built-in electric fields in BiOBr photocatalysts, Nat. Commun. 13 (2022) 2230.

Xixian Yang received his Ph.D. from South China University of Technology in June 2013. He is currently an Associate Researcher at the Institute of Biomass Engineering, South China Agricultural University, and serves as a Master's Supervisor at South China University of Technology, Guangdong University of Technology, and Guangzhou University. His research interests include the preparation of novel nanomaterials and their applications in energy storage and environmental catalysis. As a researcher, he has led several projects funded by the National Natural Science Foundation of China and other provincial-level projects, and has published numerous papers in internationally renowned journals.

Prof. **Shanqing Zhang**, is currently a distinguished Professor, National high-level talent of China, and director of the Institute for Sustainable Transformation, Guangdong University of Technology, China. He was awarded the Australia Research Council Future Fellowship for 2009–2013 and promoted to a full professor at Griffith University in Queensland during 2016–2023. He is a Fellow of the Royal Society of Chemistry (UK) and a fellow of the Royal Australia Chemical Institute. Prof. Zhang is playing an important role in bridging Australia and China in the research area of nanomaterials and functional polymers for chemical sensing, and energy storage.

Dr. **Shengsen Zhang** is a professor at South China Agricultural University, specializing in Industrial Catalysis with a Ph.D. obtained from South China University of Technology and joint Ph.D. training completed at Griffith University, Australia. His research primarily focuses on the design and fabrication of innovative photocatalytic materials for effective environmental pollution control, precise environmental monitoring, and efficient energy conversion. Dr. Zhang has authored more than 120 academic papers indexed by SCI, including publications in highly influential journals such as Advanced Materials and Advanced Functional Materials. Additionally, he holds 12 national invention patents and has successfully led 12 significant research projects funded by prestigious institutions like the National Natural Science Foundation of China.